inorganics

MDPI

Review

Nanotechnology of Positive Electrodes for Li-Ion Batteries

Xiaoyu Zhang [1], Ana-Gabriela Porras-Gutierrez [2], Alain Mauger [3], Henri Groult [2,*] and Christian M. Julien [2]

1 SynPLi Consulting, 17300 Rochefort, France; zhangxiaoyu2001@hotmail.com
2 Physicochimie des Electrolytes et Nanosystèmes Interfaciaux, Unité Mixte de Recherche 8234, Sorbonne Universités, UPMC Universités Paris6, 4 Place Jussieu, 75005 Paris, France; Ana-gabriela.porras-gutierrez@upmc.fr (A.-G.P.-G.); christian.julien@upmc.fr (C.M.J.)
3 Institut de Minéralogie, de Physique des Matériaux et de Cosmochimie, Sorbonne Universités, UPMC Universités Paris6, 4 Place Jussieu, 75252 Paris, France; alain.mauger@impmc.jussieu.fr
* Correspondence: Henri.Groult@upmc.fr

Academic Editor: Tom Nilges
Received: 1 March 2017; Accepted: 8 April 2017; Published: 14 April 2017

Abstract: This work presents the recent progress in nanostructured materials used as positive electrodes in Li-ion batteries (LIBs). Three classes of host lattices for lithium insertion are considered: transition-metal oxides V_2O_5, α-NaV_2O_5, α-MnO_2, olivine-like $LiFePO_4$, and layered compounds $LiNi_{0.55}Co_{0.45}O_2$, $LiNi_{1/3}Mn_{1/3}Co_{1/3}O_2$ and Li_2MnO_3. First, a brief description of the preparation methods shows the advantage of a green process, i.e., environmentally friendliness wet chemistry, in which the synthesis route using single and mixed chelators is used. The impact of nanostructure and nano-morphology of cathode material on their electrochemical performance is investigated to determine the synthesis conditions to obtain the best electrochemical performance of LIBs.

Keywords: transition-metal oxides; cathode materials; nanotechnology; Li-ion batteries

1. Introduction

The main drawback of transition-metal oxides used as positive electrode (cathode) materials in Li-ion batteries (LIBs) is their poor discharge rate capability due to low intrinsic electronic and ionic conductivity [1]. Thus, at high current densities, i.e., $J > 1$C rate (the rate is denoted C/n, where C is the theoretical cathode capacity and a full discharge occurs in n hours), the poor electrochemical performance is attributed to the slow electron transport of the material and the sluggish Li-ion kinetics within the grains. The currently adopted approach to get high rate capability is to reduce the diffusion path length of charge species by minimizing the particle size of the active phase [2,3]. The smaller the particle size, the larger the surface area over volume ratio, as shown in Figure 1 in which a 3×3 cube is compared to a single element. In this case, the surface/volume ratio is increased from 2 to 6.

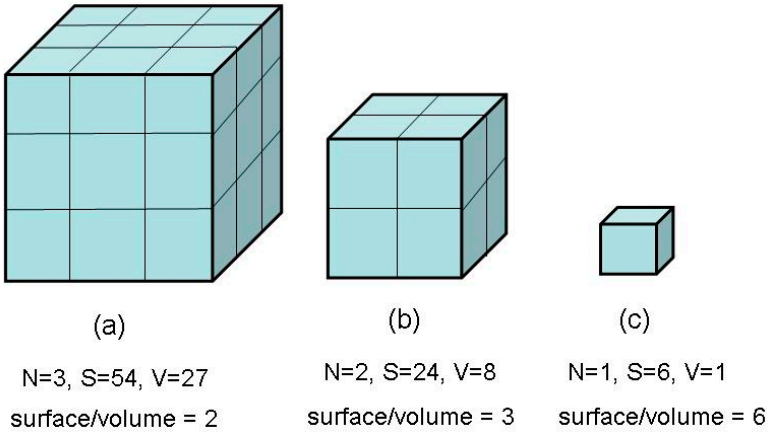

Figure 1. Representation of the evolution of the surface/volume ratio for a cubic assembly of (**a**) 3 × 3 cube; (**b**) 2 × 2 cube and (**c**) single element (N = dimension, S = surface, V = volume).

The characteristic time τ for an ionic species *i* (in practice Li^+ ions in the present case) to reach the surface of an active particle of dimension *L* is given by the relation [2]:

$$\tau_{sp} = \frac{L^2}{4\pi D*}, \quad (1)$$

$$\tau_{tp} = \frac{F^2}{2V_m} \frac{L^2}{\langle \sigma^i \rangle \Delta\mu^i}. \quad (2)$$

The first equation is the Fick's law that applies when the motion of the ion is a diffusion process, with D^* is the chemical diffusion coefficient of moving ions. Such is the case when the chemical reaction proceeds by a single phase (sp) process, i.e., within a solid solution. On another hand, in a two-phase (tp) process, where there is a separation between a Li-rich and Li-poor phase instead of a solid solution, the chemical reaction proceeds by the nucleation of the phases and motion of the propagation of the boundaries that separate the two phases. In that case, the characteristic time is given by the Equation (2), where V_m is the molar mass of the active compound, σ^i the ionic conductivity and $\Delta\mu^i$ the difference of the chemical potential of ions between the two phases. In both cases, however, τ is proportional to L^2. Therefore, by reducing the dimension *L* of the active particles of battery electrode from the micrometer to the nanometer range, one reduces the characteristic time τ for diffusion of ionic species in the solid-state phase by a factor of 10^6.

Let us estimate the characteristic time (the minimum charge duration of the battery) for a typical lithium insertion compound such as $LiFePO_4$. Taking into account the pre-factor of L^2 in the second equation, we find that τ equals 9 h for 2 μm-particle size, reduced to 13 min for 100 nm-particle size. Therefore, faster charge process requires the fabrication of particles of smaller size, $L < 100$ nm, which is a very challenging technology at the industrial scale. Okubo et al. [4] have observed an excellent high-rate capability of $LiCoO_2$ particles of 17 nm in size, since 62.5% of the capacity at 1C rate is preserved at 100C. In this context, based on the Li-ion diffusion coefficient $D^* \approx 2.5 \times 10^{-12}$ $cm^2 \cdot s^{-1}$, the discharge process within 100 s requires the particle size $L = 100$ nm against 1 h for $L = 2$ μm. Thus, 100-nm sized particles can be fully charged/discharged even at 10C rate (1.4 $A \cdot g^{-1}$). It was also demonstrated that control of the particle size can be obtained via synthetic methods, such as sol–gel [5] and hydrothermal process [6] in particular. Figure 2 lists the beneficial/detrimental effects associated with the nanotechnology of electrode materials for Li-ion batteries. In addition to the effect of the particle size and particle size distribution on the insertion mechanism, we must also consider the effect of the high specific surface area of nanoparticles (safety problems) and the minimization of the volume expansion upon Li-ion insertion.

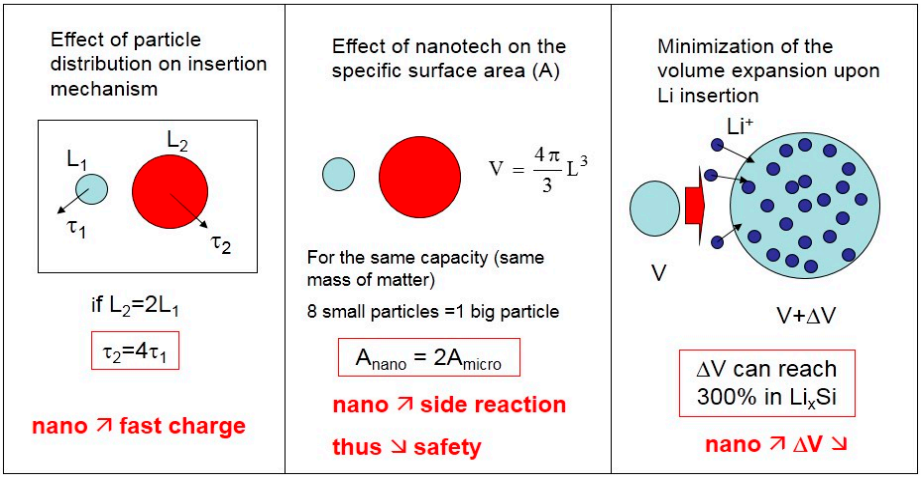

Figure 2. Beneficial/detrimental effects of nanotech of electrode materials for Li-ion batteries.

The aim of this paper is to investigate the effect of the nanotechnology on the electrochemical properties of positive electrode materials for Li-ion batteries. First, a brief description of the preparation methods shows the advantage of a green process in which the synthesis route uses single and mixed chelators. The following section is devoted to the relationship between the nanostructure and nano-morphology of cathode material and their electrochemical performance. The different host lattices for lithium insertion include: the metal oxides V_2O_5, α-NaV_2O_5, α-MnO_2, olivine $LiFePO_4$, and layered compounds $LiNi_{0.55}Co_{0.45}O_2$, $LiNi_{1/3}Mn_{1/3}Co_{1/3}O_2$ and Li_2MnO_3.

2. Synthesis of Nanomaterials

Many synthesis routes are currently used to produce nanostructured materials. The most successful techniques for the preparation of $LiFePO_4$ nanopowders include wet-chemical methods: sol–gel [7] and co-precipitation [8] because of the accessibility of cheap raw materials. Other techniques are hydrothermal route [9], template method [10] and mechanical activation [11] because it enables the control of the morphology.

The sol–gel technique consists in the formation of a solid phase via gelation of a colloidal suspension, i.e. gel. Following the conversion of sol in gel, the polycrystalline material can be formed via inorganic polymerization reactions in solution. Further drying of the gel provides "dry gel" (xerogel) state and subsequent heat treatment can be used to remove unreacted organic residues, stabilize the gel, make it denser and induce good crystallinity. The wet-chemical synthesis of transition-metal oxides for electrodes of lithium batteries leads to a high degree of homogeneity with minimum particle size in the submicron range, high surface area and good stoichiometry control due to the molecular mixing of raw materials. However, in the sol–gel method, the choice of chelators often directly affects electrochemical properties of the products. Figure 3 shows the molecular scheme of mixed chelators with different architectures, which belong to the class of bio-reagents. For example, when only citric acid is used as chelating agent, some issues will appear in the process of heat treatment due to the existence of segregation phenomenon in the precursors, such as too high heating temperature, too long calcinating time and irregular morphology of the materials [12]. On a general basis, mixing different chelators (Figure 3b) improves the structural properties and correlatively the electrochemical properties. This is due to the fact that chelating a metal ion to create a neutral compound that is needed in the synthesis process. On the other hand, some chelates can be too stable, protecting the mineral from being complexed with other precursor elements of the cathode material. The compromise can hardly be found with a single chelating agent, while it can be obtained by mixing them to add their specific properties. Let us discuss the effect of the nature of the chelating reagent on the synthesis of nanostructured α-MnO_2 by wet-chemical techniques.

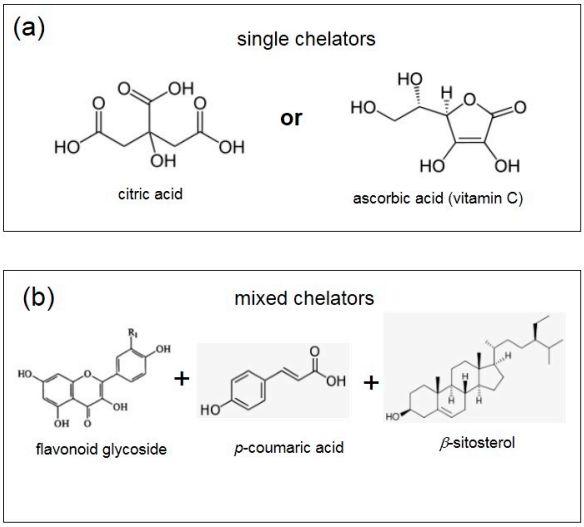

Figure 3. Molecular scheme of mixed chelators with different architectures, which belong to the class of bio-reagents. (**a**) chelators formed by a single or dual reagents, i.e. carboxylic acids; (**b**) mixed chelators including several bio-reagents with complex structure.

Figure 4 shows the X-ray diffraction (XRD) patterns for the MnO_2 nanowires prepared by the reduction of $KMnO_4$ by a carboxylic acid at 350 °C. Using ascorbic acid (vitamin C) as a single chelator, the product crystallizes in the tetragonal structure of the α-MnO_2 cryptomelane (space group *I*4/*m*) with a 2 × 2 tunnels. The mean crystallite size of the α-MnO_2 nanoneedles is L_c = 14 nm [13]. The same material prepared by a green technique using a mixed chelator composed by bio-reagents such as those that exhibit a smaller crystallite size of 6.4 nm, which results in primary nanorods of ~17 nm in diameter and 84 nm in length. Slight modifications of the synthesis recipe induce different morphologies of nanostructured α-MnO_2; for instance, sea-urchin-like shape, with a diameter of ~3 μm, were prepared in acidic conditions [13], while a neutral medium provided a caddice-clew-like MnO_2 showing lower electrochemical performance [14]. The use of mixed chelator has been successful for the growth of Li-riche layered compounds. The $Li[Li_{0.2}Ni_{0.2}Mn_{0.6}]O_2$ oxide was prepared by a combined citric acid (CA) and an ethylenediamine tetraacetic acid (EDTA) route. Typically, CA and EDTA dissolved in NH_4OH was added to a solution containing requested stoichiometry of metal acetate. The viscous gel was formed at ~120 °C and the final product heated at 850 °C for few hours. Note the crucial importance of the acid/metal ratio, which in the present case is 1.5:1:1 to keep the nanostructure [15].

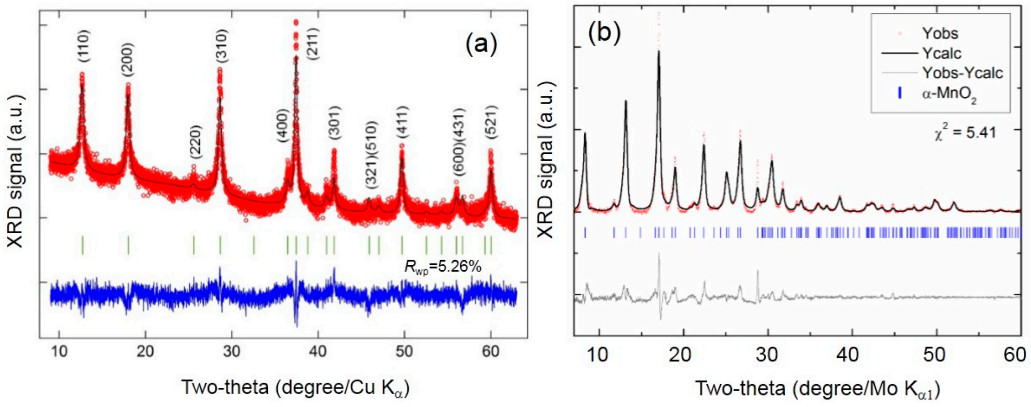

Figure 4. XRD patterns for (**a**) α-MnO_2 nanoneedles prepared by the reduction of $KMnO_4$ using the single ascorbic-acid route and (**b**) α-MnO_2 nanowires prepared using the mixed chelator shown in Figure 3b. Copyright permission from Springer.

Precipitation processes are among the oldest of techniques for the synthesis of nanomaterials that consist of the condensation of a solid oxide network (the precipitate) starting from soluble species. The condensation of the species is initiated by a redox reaction or by a change of pH. The preparation of nanocrystalline powders can be realized by co-precipitation using inorganic media for polymerization in aqueous solution. This method was successful to synthesize $LiNi_xMn_yCo_{1-x-y}O_2$ layered oxides [16]. During the synthesis of $LiNi_{1/3}Mn_{1/3}Co_{1/3}O_2$, the lithium/transition-metal ratio and calcination temperature were adjusted to minimize the cation mixing and optimize its electrochemical performance. Succinic acid is used for the formation of a chelation complex to prevent the segregation or precipitation of metal ions. The acetate ligand, succinic acid, has oxygen atoms and hydrogen atoms that can participate in hydrogen bonding. As a result, metal acetates are trapped in a glassy state by an extended network of hydrogen bonds. At the same time, succinic acid complexes to the metal acetates and replaces the water of hydration in the complex to give acid–acetate species [17]. Succinic acid also acts as fuel and provides local heat for the formation of the compound during the decomposition process owing to its self-igniting property, thus accelerating the decomposition of acetate ions. The sketch of the synthesis of by succinic-assisted co-precipitation is shown by the thermogravimetry curve (Figure 5), in which we observed the decomposition of the organic moieties and the beginning of the powder crystallization at temperature as low as 376 °C.

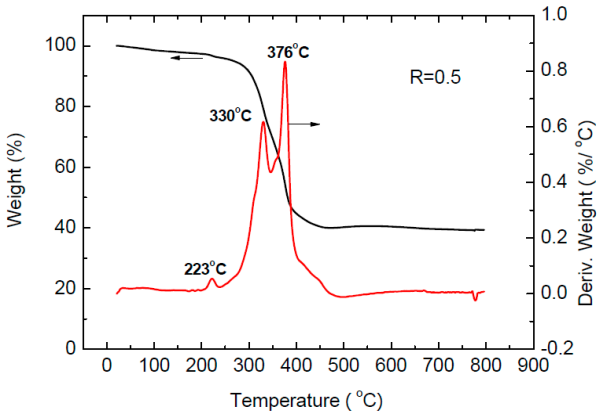

Figure 5. Thermogravimetric analysis profile for the precursor of $LiNi_{1/3}Mn_{1/3}Co_{1/3}O_2$ synthesized with acid to metal ion molar ratio of R = 0.5 showing the ignition at 376 °C.

For more than 100 years, hydrothermal synthesis was clearly identified as an important technology for preparation of nanometer-sized particles that can be quenched to form a nanoparticle powder, or cross-linked to produce nanocrystalline structures [18]. Among the various synthesis approaches pursued in the fabrication of electrode materials for Li-ion batteries, the hydrothermal route is particularly successful to control the chemical composition, crystallite size, and particle shape [9]. With respect to the previous techniques, the hydrothermal process has the advantage that the synthesis temperature can be as small as 230 °C and a duration of reaction of 5–12 h. The use of hydrothermal route will be emphasized for the optimization of lithium iron phosphate.

The template method consists of a thermal decomposition of the sol–gel precursor within the pores of a membrane. The template is dipped into the sol for 10 min and taken out for heating at T > 400 °C, resulting in the formation of the nanomaterial within the template pores. This technique has the advantage of monitoring the pore size [19], so that the morphology can be adapted to optimize the electrochemical properties. However, the preparation of nano-structured materials from the template synthesis techniques uses polycarbonate filtration membranes followed by removal of substrates. One of the disadvantages of the template method is related to high cost and complicated synthetic procedures that are difficult to expand to mass production. Consequently, a template-free reverse micelle process was utilized for the synthesis of rodlike C-$LiFePO_4$ particles [20].

The drawback of the solid-state reaction is the lengthy procedure of calcination that leads usually to bigger particles, and already reported above this is at expense of the rate capability. In the mechanical activation (MA) method, a high energy ball milling step is introduced before thermal treatment. This step aims at forming an intimate mixture of the reactants that effectively reduces the thermal treatment time and temperature, thus arresting the undesirable crystal growth. Some studies have highlighted the effectiveness of MA process for the synthesis of small and phase-pure particles of $LiFePO_4$ [21–23] and C-$LiFePO_4$ [24]. Even with a limited amount of carbon (2 wt %) appropriate for commercial batteries, the capacity of $LiFePO_4$ obtained after jet milling and wet milling reached 157 $mAh{\cdot}g^{-1}$ at 0.1C, 120 $mAh{\cdot}g^{-1}$ at 10C, without capacity fading after 60 cycles [21]. A review on the synthesis of nanosized electrode materials with layered and spinel structure by mechanical activation and studies of their properties can be found in [25]. The mean particle size obtained in this process is 50–200 nm. To prevent the particles coarsening during the MA, the MA can be realized in the presence of inert compound. In particular, $LiCoO_2$ powder with grain size 50 nm was obtained by such a technique [26]. Note, however, that the milling process can deteriorate the surface layer. It is thus important to check that the thermal treatment after the milling cures the problem by re-crystallizing the surface layer. In addition, there is a tendency of the nanoparticles to agglomerate to form typically 100 nm-thick secondary particles.

The mechano-fusion is an efficient way to coat the particle. Here, the smaller particles of the coating material are projected on the larger particles of the active element that have been already synthesized, in order to anchor the coating particles on the surface of the active particles. This process was used to coat $LiMn_{1.5}Ni_{0.5}O_4$ with $LiFePO_4$, which was impossible via the traditional sol–gel method. The $LiFePO_4$ formed a protective layer against the electrolyte [27], which improved significantly the electrochemical properties. In addition, the coating particles were also electrochemically active in this case.

3. Electrochemistry of Nanostructured Cathodes

As a general rule, the electrochemical properties of cathodes are governed by the microstructure of the material, especially the local environment of active redox centers, i.e., the transition metal ions in cathode oxides. Thus, the long range order favors the formation of well-defined phases upon lithium insertion, while short range order modified deeply the charge–discharge profiles with absence of phase transition, i.e., formation of voltage plateaus [1]. In the following, we present several examples that emphasize the properties of nanomaterials used as cathodes in lithium batteries.

3.1. Thermodynamic Approach

For a given redox couple, the potential of an intercalation electrode considered as solution of guest *A* in the host lattice <*H*> is provided by the classical thermodynamic law:

$$V(x) = -\frac{1}{zF}\frac{\partial(\Delta G)}{\partial x} + constant, \quad (3)$$

where ΔG denotes the variation in the Gibbs energy of the system, x is the composition, z the number of electrons involved and F the Faraday's constant. $V(x)$ is thus the electrode potential as a function of the composition x in the moving ionic species. If the particles contain two phases (Figure 6a), the system has no degree of freedom, implying that the derivative $\partial(\Delta G)/\partial x$ is a constant and the cell potential cannot change during the chemical reaction. A wide voltage plateau is observed in the composition range $\alpha_1 \leq x \leq \beta_1$ as shown in Figure 6b. A general feature is the fact that the insertion or de-insertion process for the Li_xMPO_4 (M = Fe, Co, Ni) olivine materials is a two-phase process at temperature of interest. It means that, for instance, the Li_xFePO_4 solid solution does not exist unless x is close to zero or close to 1. As a consequence, a rapid de-mixing occurs, and we are left with a two-phase system, namely, $Li_{1-\alpha}FePO_4$ (Li-rich) and $Li_\beta FePO_4$ (Li-poor). The compositions α and β denote the width of the single-phase region in Figures 6 and 7. For micrometer-sized particles (energy grade material), $\alpha \approx \beta \approx 0$, that provides the chemical formula of the bulk material at intermediate concentrations

under the form xLiFePO$_4$ + (1 − x)FePO$_4$ (Figure 6b). For nanometer-sized particles (power grade material), the Gibbs energy varies according to the scheme represented in Figure 7a, and the two-phase domain is reported to shrink. Accordingly, the voltage plateau is shorter due to the larger values of α and β that result in the shrinking of the single-phase regions [1]. The corresponding voltage profile for the Li//LiFePO$_4$ half-cell with nanosized cathode particles shown in Figure 7b displays a reduced voltage plateau over the concentration range $\alpha_2 \leq x \leq \beta_2$ with $\alpha_2 > \alpha_1$ and $\beta_2 > \beta_1$.

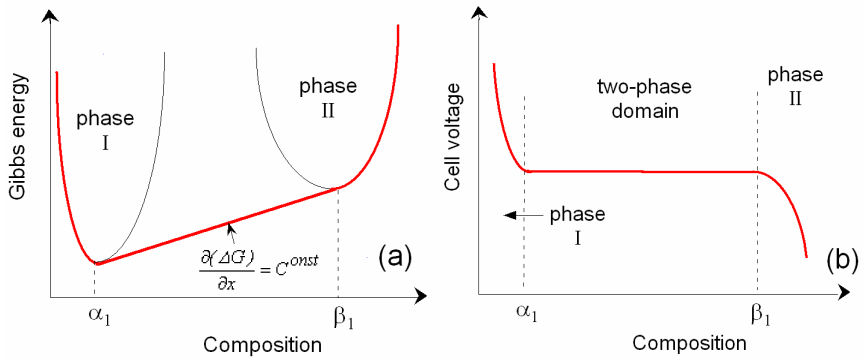

Figure 6. (**a**) schematic representation of the Gibbs rule for a two-phase system; (**b**) the cell voltage profile shows a plateau in the composition range $\alpha_1 \leq x \leq \beta_1$ for the bulk material.

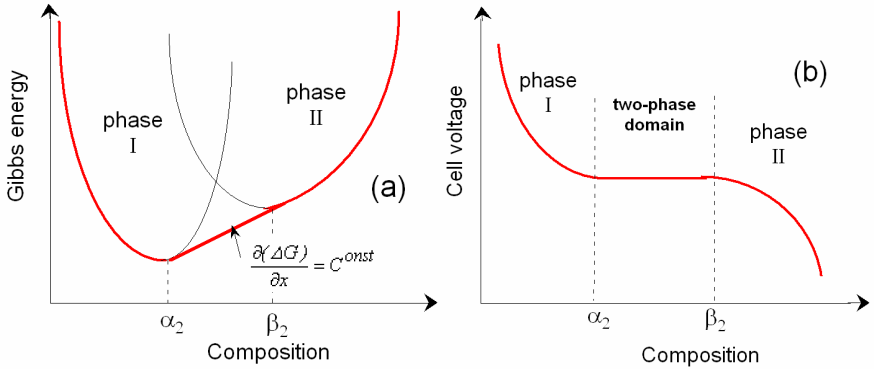

Figure 7. (**a**) schematic representation of the Gibbs rule for a two-phase system; (**b**) cell voltage vs. composition for nano-sized material.

3.2. Transition Metal Oxides

3.2.1. Vanadium Pentoxide

V_2O_5 has received considerable attention due to its high theoretical specific capacity ~440 mAh·g^{-1} when 3Li$^+$ ions are inserted [28]. Here, we compare the properties of micron-sized and nanostructured V_2O_5 samples with the morphology shown by the transmission electron microscopy (TEM) images in Figure 8. V_2O_5 was grown by the decomposition of ammonium metavanadate (NH_4VO_3) at 220 °C. The product shows a good crystallinity (Figure 8a). Vanadium bronzes $Na_yV_2O_5$ with the needle-like morphology were synthesized via the hydrothermal route from a mixture of V_2O_5 and NaOH in the presence of ethanol as reducing agent (Figure 8b). The structure of the α'-$Na_yV_2O_5$ phase ($0.7 \leq y \leq 1.0$) is close to that of V_2O_5. It is built of [V_2O_5] layers separated by Na^+ ions. Nanostructured thin films of V_2O_5 deposited on Si(100) substrate were obtained by pulse laser deposition (PLD) [29]. For a substrate maintained at 500 °C, the grain size of PLD films is ~80 nm (Figure 8c). One of the principal properties of the films obtained by PLD is the high density compared with films grown by classical techniques.

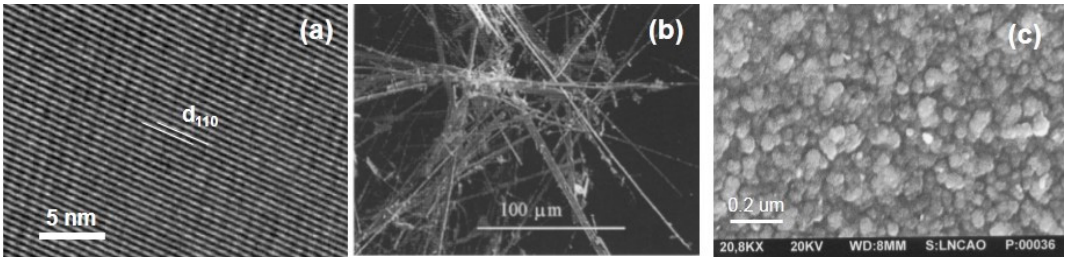

Figure 8. (**a**) TEM image of a crystalline 6 µm-V_2O_5 prepared by solid state reaction; (**b**) needle-like α′-$Na_yV_2O_5$ synthesized via the hydrothermal route with ethanol as complexing reagent and (**c**) V_2O_5 film prepared by PLD technique with 80 nm grain size.

Figure 9 shows the discharge curves of three $Li_xV_2O_5$//Li cells including the electrodes described above. The discharge profile of crystalline micron-sized $Li_xV_2O_5$ (1 µm-particle size) is rather complex, showing three plateaus due to the appearance of several structural phases: the α-phase is formed at $x < 0.01$ followed by the ε-phase ($0.35 < x < 0.7$) and then the δ-phase. For further Li insertion, $x > 1$, a permanent structural modification occurs leading to the γ-phase, which can be cycled in the range $0 \leq x \leq 2$ [28]. Bouhedja et al. [30] was the first group to show the reversible lithium intercalation within the α′-$Na_yV_2O_5$ nanoneedle structure. Similarly to V_2O_5, the quasi-1D, needle-like structure α′-$Na_yV_2O_5$ exhibits a stepwise discharge behavior during the insertion of Li. Three well-defined regions are observed in the discharge curve of $Li_xNaV_2O_5$ in the range $0 \leq x \leq 2$ (Figure 9). In this compositional domain, the discharge curve corresponds to the voltage profile characteristic of the needle-like crystal associated with the occupation of the octahedral sites by Li. The first region extends up to 0.12 e^- per vanadium, the second one (with an S-shape behavior) up to 0.6 e^- per vanadium, and the third one up to 1.0 e^- per vanadium. Above $x = 0.4$ in $Li_xNaV_2O_5$, the voltage decreases smoothly down to 1.5 V with a slope of 0.52 V·mol^{-1}. From the electro-neutrality point of view, the intercalation of Li^+ ions in the $Li_xNaV_2O_5$ lattice should lead to the quantitative reduction of V^V into V^{IV} and V^{III} valence states giving the vanadium bronze $Li_2NaV_2O_5$ [30]. From the structural point of view, it may be inferred that the fibrous morphology of NaV_2O_5 needles allows fast Li^+ ion diffusion in the solid phase. The effect of the nanostructure is clearly evidenced in the discharge curve of PLD V_2O_5 film electrodes. For small particle size, the free Gibbs energy of V_2O_5 nanostructured grains is remarkably modified; thus, the modified Gibbs energy plus the presence of amorphous grain boundaries provide a smooth discharge profile from 3.5 to 0.5 V vs. Li^+/Li° in the whole $Li_xV_2O_5$ composition ($0 \leq x \leq 2$) as the cell potential $V(x)$ is the derivative $\partial(\Delta G)/\partial x$.

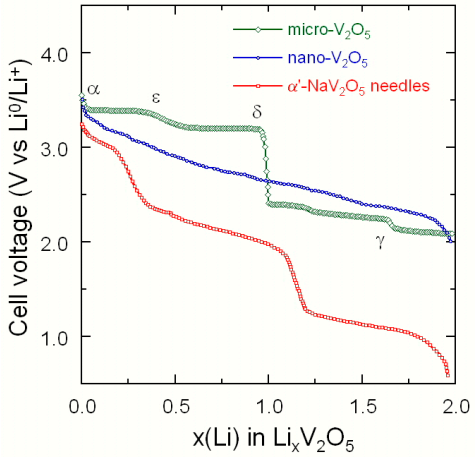

Figure 9. Discharge profiles of $Li_xV_2O_5$ electrodes recorded at room temperature at C/48 rate in Li cells with 1 mol·L^{-1} $LiClO_4$ in PC as electrolyte.

3.2.2. Manganese Dioxide

Cryptomelane α-MnO_2 polymorph is an attractive electrode material for lithium batteries due to its low cost, environmental friendliness and natural abundance but suffers from low electronic conductivity [31,32]. Nanotechnology has recently been employed as another route to enhance the electrochemical properties of MnO_2 cathode materials for rechargeable batteries [33–35], so that capacities of ca. 250 mAh·g^{-1} can be reached [36]. Nanostructured Li_xMnO_2 with with 2 × 2 tunnels is a stable material over a wide range of lithiation concentration. α-MnO_2 can be used as a cathode or anode in the potential range 3.5–1.5 V and 1.5–0 V vs. Li^+/Li^0, respectively. Several studies gave evidence of the importance of inserted cations for enhancing structural stability of α-MnO_2 [37,38]. The structure stabilization by the chemical insertion of two Li-ions per unit cell, thus improving the initial discharge capacity, has been demonstrated by Kijima et al. [37] during cycling. Stable cycling performance of α-MnO_2 has also been reported for samples prepared by hydrothermal–electrochemical synthesis [39]. Due to the renewed interest of α-MnO_2, we investigated the structural stability of its lithiated phase in the potential range 3.5–1.5 V vs. Li^+/Li^0, when prepared as nanoneedles after the reduction of $KMnO_4$ by the ascorbic acid (AA) route, and nanowires prepared by the mixed chelator (MC). Detailed XRD patterns are reported in Figure 4.

The galvanostatic discharge–charge profiles of Li//α-MnO_2 cells are characterized by the following features: (i) the first cycle is dominated by a distinct irreversible capacity loss $C_{loss} \approx 35$ mAh·g^{-1} for both materials; (ii) the degree of crystallinity affects the shape of discharge–charge profiles; (iii) the discharge and charge plateaus are clearly observed in highly crystallized MC-MnO_2 sample, while the discharge–charge curves AA-MnO_2 display a rather S-shape characteristic of a disordered material. The initial discharge capacity of AA-MnO_2 sample is 245 mAh·g^{-1}, larger than that of the MC-MnO_2 (214 mAh·g^{-1}). This can be attributed to the smaller size of the particles of the AA-MnO_2 that results in an increased effective interface between the material and the electrolyte, but as soon as the second cycle is finished, the situation is reverse. Figure 10 presents the Peukert plots of nanostructured α-MnO_2 electrodes, i.e., the specific capacity as a function of the rate capability for discharge–charge current density in the range from 10 to 400 mA·g^{-1} (1C = 260 mA·g^{-1}). These results shows the better electrochemical performance of MC-MnO_2 that provides evidence of the importance of its synthesis recipe.

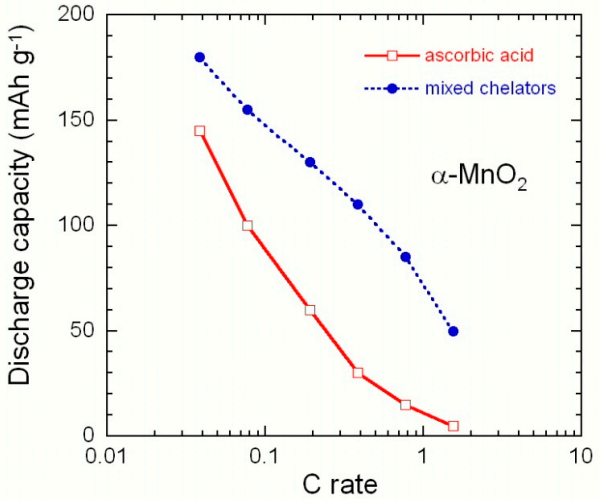

Figure 10. Peukert plots of the nanostructured α-MnO_2 electrodes prepared by different wet-chemical methods: single and mixed chelators.

3.3. Olivine-Like Materials

Li*M*PO_4 (*M* = Fe, Mn) olivine materials used as electrodes of high-power sources (in hybrid electric vehicles, for instance) request an increase of rate capability that could be achieved by reducing the particle size of electrochemically active materials. The decrease as much as possible of the size of the particles has two effects; first, it increases the effective electrode-electrolyte contact that is the active interface for electrochemical reactions, secondly, it reduces the pathway for electrons and lithium ions inside the bulk. Consequently, the electronic and ionic conductivity are small [40], this reduction is expected to be beneficial to the performance, especially at high C-rates. The experimental results, however, are not as simple as one might have expected because the reduction in size implies that surface effects become more important, and the surface layer does not necessarily have the same properties as the bulk, which impacts the electrochemical properties. The bulk properties (i.e., physical and chemical properties of particles big enough so that surface effects are negligible) are now well understood. This is not the case, yet, for surface effects that are still under debate.

Several experiments have provided evidence of the existence of a disordered layer (DSL) at the surface of particles of oxide [41], typically in a surface layer a few nanometers thick, which modified the intrinsic properties of electrode material for Li-ion batteries [41,42]. However, the quality of the particle surface state and particle morphology are primordial, because the surface-to-volume ratio increases for nanomaterials (see Figure 1) that prevents the surface to act as a barrier for lithium ions and electrons during the charge and discharge process of lithium batteries. Figure 11 depicts a simple model of the shell-core volume ratio, R_{SC}, for a 5-nm thick surface layer: in the case of a big enough particle (0.5 µm diameter) R_{SC} = 3%, while it becomes 49% for 25 nm diameter nanoparticle. In this context, it is obvious that the nanoparticle behaves differently than the big one. The strong dependence of the surface chemistry of active particles on the capacity retention of cathode materials has been suggested by Aurbach et al. [43]. It was states that any particles of the insertion compound, are always covered by a surface film that limits the migration of Li-ions and the charge transfer across the active interface. This can be evidenced by high-resolution transmission electronic microscope (HRTEM) images, which show a surface layer (SL) of about 2 nm thick. Generally, the SL is strongly disordered, but not amorphous [41]. HRTEM experiments display the core of the particles below the surface that has a size similar to the coherence length deduced from the XRD analysis. Therefore, the particles are well crystallized surrounded by a disordered surface layer (DSL). Figure 11 displays the scanning electron microscopy (SEM) images of two types of LFP particles: one was synthesized by solid-state reaction via the polymer-precursor method showing particles of 2–5 µm size, and the other one was synthesized by hydrothermal method showing particles with an average size of 300 nm. The modified Peukert plots for these two electrode materials are shown in Figure 12. It is remarkable that the power-grade powders retained 75% of the initial capacity at 10 C-rate.

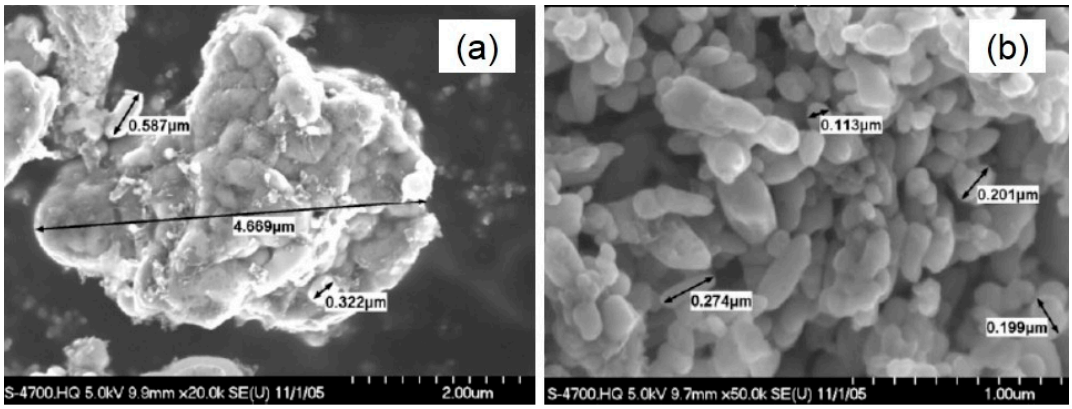

Figure 11. SEM images of $LiFePO_4$ powders. (**a**) energy grade and (**b**) power grade powders.

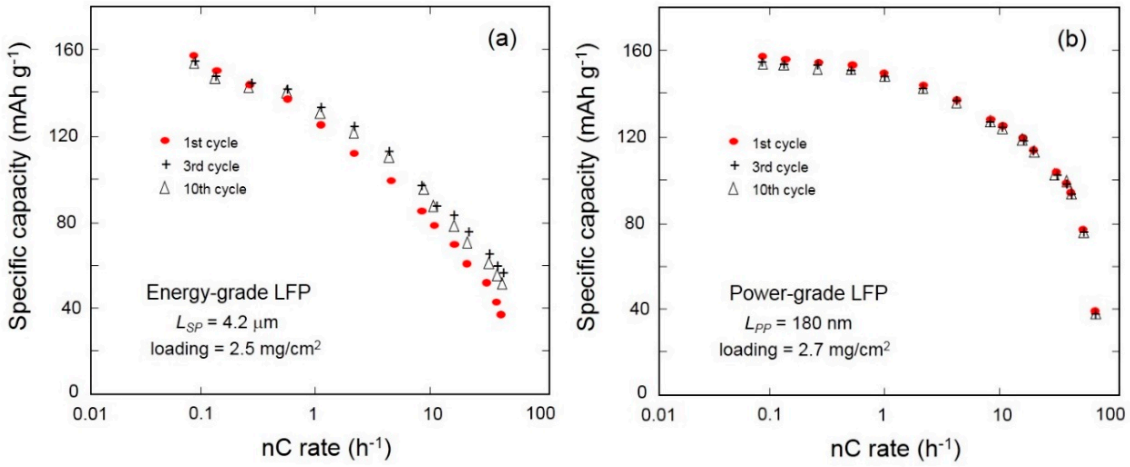

Figure 12. Modified Peukert plots of $LiFePO_4$ cathode materials as a function of the particle size: (**a**) energy grade and (**b**) power grade powders.

3.4. Layered Structures

3.4.1. Layered $LiNi_{0.55}Co_{0.45}O_2$

A typical example describing the particle size effect is provided by the synthesis of $LiNi_{0.55}Co_{0.45}O_2$ (NCO). Figure 13 shows the HRTEM images of NCO particles with different particle sizes: (**a**) nanometric particles, 100–150 nm average size, prepared by hydrothermal method and (b) micron-sized material, 1.5–2.0 µm particle size, was prepared by a two-step co-precipitation technique. The good crystallinity of powders is shown by the electron diffraction diagram (insert). The discharge capacity curves of the corresponding $Li//LiNi_{0.55}Co_{0.45}O_2$ coin-type cells as a function of C-rate are presented in Figure 14. An obvious difference in the electrochemical performance is evidenced. The Li cell with nanosized particles allows a specific capacity 150 $mAh{\cdot}g^{-1}$ for a 1C discharge rate, which is twice the capacity of the cell with micro-sized particles. The excellent rate capability makes nano-$LiNi_{0.55}Co_{0.45}O_2$ suitable electrode materials for high power application. Remark that the architecture of the electrode material at the sub-micron scale (regular particle morphology, particle distribution, absence of agglomerates) favors the cycling life of battery and the accommodation of volume changes caused by Li^+ ions insertion/extraction into/from the single particle due to faster stress relaxation.

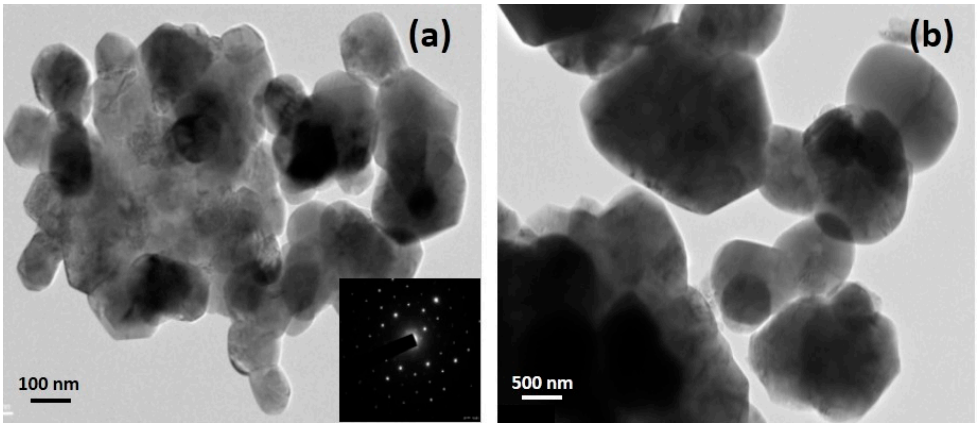

Figure 13. HRTEM images of $LiNi_{0.55}Co_{0.45}O_2$ layered powders with different particle sizes: ca. 100–150 nm (**a**) and 1.5–2.0 µm (**b**). The good crystallinity of powders is shown by the electron diffraction diagram (insert).

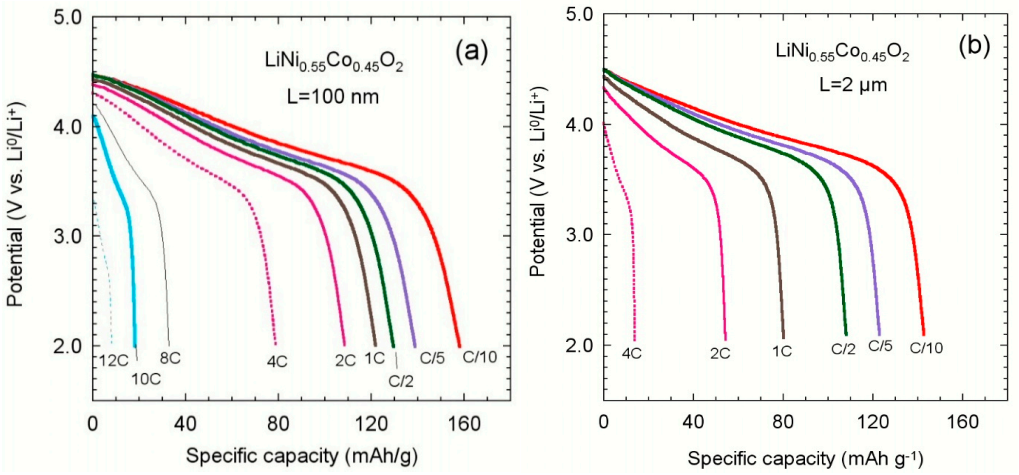

Figure 14. Discharge profiles as a function of C-rate for Li//$LiNi_{0.55}Co_{0.45}O_2$ coin-type cells with two cathode materials of 100 nm and 2 µm particle size.

3.4.2. Layered $LiNi_{1/3}Mn_{1/3}Co_{1/3}O_2$

Actually, not even the transition-metal oxides, but also carbon coating is efficient to improve the cycle life of Li-ion batteries with $LiN_{1/3}Mn_{1/3}Co_{1/3}O_2$ (NMC) and $LiCoO_2$ (LCO) as well. An annealing effect re-crystallizes the surface layer that is otherwise disordered. This is currently obtained even performing a simple heating in the presence of an organic compound. Hashem et al. [44] have studied the surface of NMC particles for material synthesized at 900 °C by a two-step process using a mixture of $LiOH{\cdot}H_2O$ and metal oxalate $(Ni_{1/3}Co_{1/3}Mn_{1/3})C_2O_4$ obtained by co-precipitation. The effect of the heat treatment at 600 °C with organic substances, i.e. sucrose and starch, was investigated. HRTEM images and Raman scattering (RS) spectra indicate that the surface of particles has been modified with heating. Any carbon coating was grown with the annealing process but a remarkable crystallization of the thin disordered layer on the surface of NMC was performed. The analysis of the HRTEM images (Figure 15) evidences the modification of the surface of particles upon calcination at 600 °C. Figure 15a shows the presence of an amorphous-like layer, typically 2.5-nm thick, that covers the NMC particle before carbon treatment. The micrograph clearly displays this surface layer that appears as a greyish region at the edge of the NMC crystallites, while the core of the primary particle is the dark region. The disappearance of the disordered layer is observed (Figure 15b) after the annealing process at moderate temperature using an organic substance such as sucrose or starch. As shown in the insert of Figure 15, the edge of the particle displays well-defined diffraction patterns. The beneficial effect has been tested on the electrochemical properties of the NMC cathode materials in half lithium cells. For rate performance comparison, the modified Peukert plots, i.e., the specific capacity vs. C-rate, are shown in Figure 16. A capacity 107 $mAh{\cdot}g^{-1}$ is delivered in the voltage range 2.5–4.2 V at a 10 C rate from the cell with surface-modified NMC, while it is only 81 $mAh{\cdot}g^{-1}$ with the non-treated NMC electrode at the same C-rate.

3.4.3. Rock-Salt Li_2MnO_3

The layered compound Li_2MnO_3 (or $Li[Li_{1/3}Mn_{2/3}]O_2$), which has an O3 structure built of close-packed oxygen layers in an *ABCABC* stacking of atoms (monoclinic structure, space group $C2/m$) is one of the most interesting compounds from the point of view of its structure and electrochemical behavior [45]. Indeed, in its microcrystalline form, this oxide was initially considered as an electrochemically inactive material in the potential range 2.0–4.4 V because no empty sites are available for Li insertion, and because of the +4 valence state of octahedrally coordinated Mn cations. However, this hypothesis has been disproved by Kalyani et al. [46]. In its nanostructured form, Li_2MnO_3 can deliver a theoretical capacity as high as 400 $mAh{\cdot}g^{-1}$ for total Li extraction. Figure 17

compares the XRD patterns of nano-sized Li_2MnO_3 material with that of micron-sized Li_2MnO_3 material. The nano-sized material is characterized by significant broadening of the peaks.

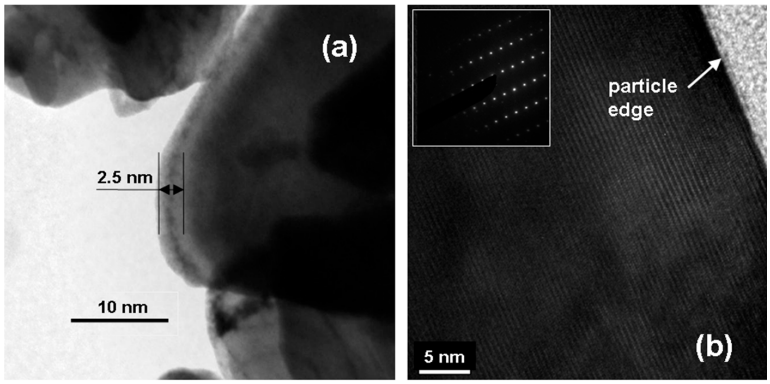

Figure 15. TEM images of NMC powders showing the surface modification of 250-nm sized particle. Images (**a**,**b**) display the HRTEM features of NMC powders for as-grown and heat treated samples with sucrose at 600 °C for 30 min in air, respectively. Copyright permission from Elsevier.

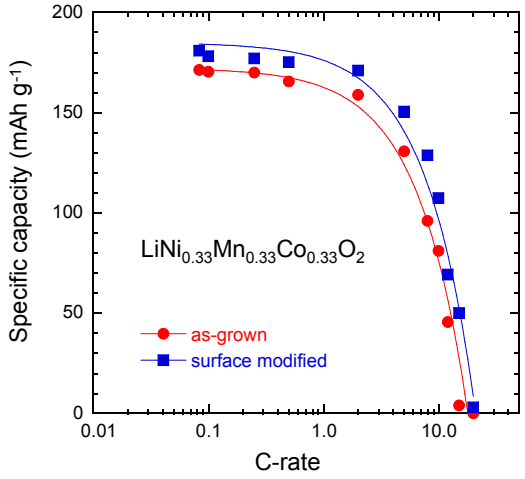

Figure 16. Modified Peukert plots of Li//NMC coin cells for the as-grown and the surface modified NMC cathode material. Copyright permission from Elsevier.

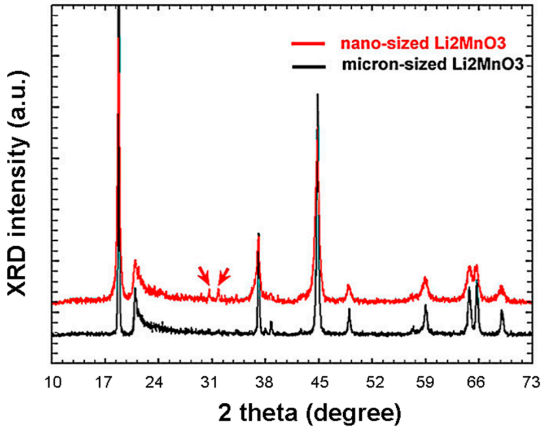

Figure 17. XRD patterns of nano-sized Li_2MnO_3 (upper curve) compared with micron-sized material (lower curve). Two peaks marked by arrows at 2θ = 30.5 and 31.6° belong to Li_2CO_3 impurity that can be formed during the synthesis due to some excess of the lithium.

Nano-particles (20–700 nm) of Li_2MnO_3 synthesized using the co-preparation method show the electrochemical activity reported in Figure 18. The strong effect of the size of particles is clearly evidenced; with the increasing synthesis temperature, the particles are bigger and bigger, resulting in a decreasing electrochemical activity. This is an opposite phenomenon observed currently in transition metal oxides such as NMC compounds.

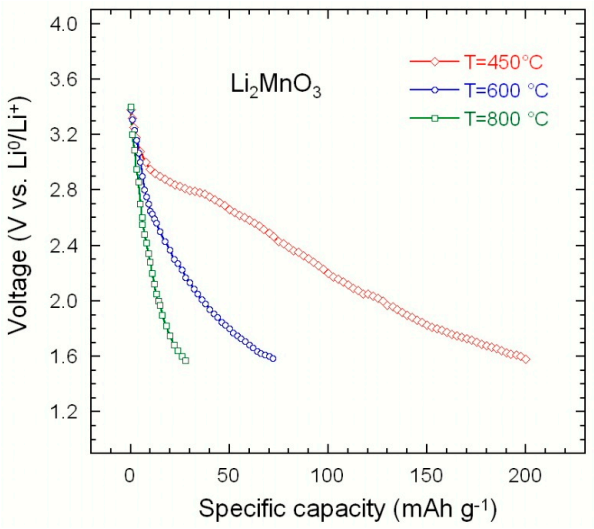

Figure 18. Discharge curves of Li_2MnO_3 prepared at different synthesis temperatures (450–800 °C) showing the strong effect of nanoparticle size.

4. Conclusions

The success in the lithium-ion batteries is greatly indebted to the development of the nanotechnology. In particular, high power applications require active particles on the order of 100 nm in size, with well-controlled crystallinity. The choice of the synthesis processes and the adjustment of the synthesis parameters were used to tune not only the size of the particles, but also their morphology in order to have optimized electrochemical properties. The choice of the active cathode elements that belong to the two families of materials (layered and olivine-like structures) to which belong the active elements of the cathodes in the lithium-ion batteries today exemplifies the crucial dependence of the electrochemical properties and the size and morphology of the particles.

In this paper, we have reported the impact of nanostructure and nano-morphology of several cathode materials on their electrochemical performance. Transition-metal oxides including nano V_2O_5, needle-like vanadium bronzes $Na_yV_2O_5$ showed the absence of stepwise voltage observed for V_2O_5 bulk. For small particle size, the free Gibbs energy of V_2O_5 nanostructured grains is remarkably modified; thus, the modified Gibbs energy plus the presence of amorphous grain boundaries provide a smooth discharge profile from 3.5 to 0.5 V vs. Li^+/Li^0 in the whole $Li_xV_2O_5$ composition ($0 \leq x \leq 2$) as the cell potential $V(x)$ is the derivative $\partial(\Delta G)/\partial x$. The electrochemical performance of the α-MnO_2 hollandite/cryptomelane structure appeared to be strongly dependent on the synthesis procedure, i.e., chelating agent used in the wet-chemistry method. It is well known that large K^+ cations are inserted into the tunnel cavity (2*a* Wyckoff site) during synthesis of this compound. The presence of K^+ is the key parameter, which governs the properties of these materials. The role of cations inside 2×2 tunnels has three beneficial effects: (i) increase of the electronic conductivity of the host; (ii) improve the Li^+ diffusivity and (iii) introduce a structural transition during lithiation for high K^+ concentration, i.e., $x = 0.25$. This large cation is essential for the formation and stabilization of α-MnO_2 lattice and leads to the mixed valence state of Mn^{4+} and Mn^{3+} ions that depends on the potassium concentration. K^+ ions increase the concentration of less-localized e_g *d*-electrons of the Mn^{3+} ions.

In the case of olivine materials LiMPO_4 (M = Fe, Mn, Co, Ni), the increase of rate capability (for use in hybrid electric vehicles, for instance) is achieved by decreasing as much as possible the size of the particles ($L \approx 40$ nm) to improve the effective surface. Since the electronic and ionic conductivity of olivine frameworks are small ($\sigma_e << 10^{-12}$ S·cm^{-1}), the nanosize is expected to be beneficial to the performance, especially at high C-rates. It is remarkable that the power-grade powders retained 75% of the initial capacity at 10C rate. Typical examples describing the particle size effect of layered materials are provided by $LiNi_{0.55}Co_{0.45}O_2$ (NCO) and $LiN_{1/3}Mn_{1/3}Co_{1/3}O_2$ (NMC) cathodes. However, improvement of the electrochemical performance (cycling stability) requests a modification of the surface of particles (coating by metal oxide) to prevent the transition-metal ion dissolution. The beneficial effect has been tested on the properties of the NMC cathode materials in half cells. It was shown that the electrochemical activity of the nanocrystalline Li_2MnO_3 electrodes depends upon the particles morphology, specific surface area, and annealing temperature of the as-prepared material, while microcrystalline powders are electrochemically inactive.

Acknowledgments: The authors thank the Université Pierre et Marie Curie (Paris 6) for financial support.

Author Contributions: Xiaoyu Zhang and Ana-Gabriela Porras-Gutierrez performed the synthesis and accomplished the measurements of materials; Henri Groult and Alain Mauger contributed to interpretation and finalized the manuscript; and Christian M. Julien led the over-arching research project.

Conflicts of Interest: There is no conflict of interest related to this document.

References

1. Julien, C.M.; Mauger, A.; Vijh, A.; Zaghib, K. *Lithium Batteries: Science and Technology*; Springer: Heidelberg, Germany, 2016.
2. Zaghib, K.; Mauger, A.; Julien, C.M. *Rechargeable Batteries*; Zhang, Z., Zhang, S.S., Eds.; Springer: Heidelberg, Germany, 2015.
3. Yamada, A.; Chung, S.C.; Hinokuma, K. Optimized $LiFePO_4$ for lithium battery cathodes. *J. Electrochem. Soc.* **2001**, *148*, A224–A229. [CrossRef]
4. Okubo, M.; Hosono, E.; Kim, J.; Enomoto, M.; Kojima, N.; Kudo, T.; Zhou, H.; Honma, I. Nanosize effect on high-rate Li-ion intercalation in $LiCoO_2$ electrode. *J. Am. Chem. Soc.* **2007**, *129*, 7444–7452. [CrossRef] [PubMed]
5. Castro-Couceiro, A.; Castro-Garcia, S.; Senaris-Rodriguez, M.A.; Soulette, F.; Julien, C. Effects of the aluminum doping on the microstructure and morphology of $LiNi_{0.5}Co_{0.5}O_2$ oxides. *Ionics* **2002**, *8*, 192–200. [CrossRef]
6. Vediappan, K.; Guerfi, A.; Gariépy, V.; Demopoulos, G.P.; Hovington, P.; Trottier, J.; Mauger, A.; Julien, C.M.; Zaghib, K. Stirring effect in hydrothermal synthesis of nano C-$LiFePO_4$. *J. Power Sources* **2014**, *266*, 99–106. [CrossRef]
7. Dominko, R.; Bele, M.; Gaberscek, M.; Remskar, M.; Hanzel, D.; Goupil, J.M.; Pejovnik, S.; Jamnik, J. Prorous olivine composites synthesized by sol–gel technique. *J. Power Sources* **2006**, *153*, 274–280. [CrossRef]
8. Wang, Y.; Sun, B.; Park, J.; Kim, W.S.; Kim, H.-S.; Wang, G. Morphology control and electrochemical properties of nanosize $LiFePO_4$ cathode material synthesized by co-precipitation combined with in situ polymerization. *J. Alloys Compd.* **2011**, *509*, 1040–1044. [CrossRef]
9. Brochu, F.; Guerfi, A.; Trottier, J.; Kopec, M.; Mauger, A.; Groult, H.; Julien, C.M.; Zaghib, K. Structure and electrochemistry of scalling nano C-$LiFePO_4$ synthesized by hydrothermal route: complexing agent effect. *J. Power Sources* **2012**, *214*, 1–6. [CrossRef]
10. Doherty, C.M.; Caruso, R.A.; Smarsly, B.M.; Drummond, C.J. Colloidal crystal templating to produce hierarchically porous $LiFePO_4$ electrode materials for high power lithium ion batteries. *Chem. Mater.* **2009**, *21*, 2895–2903. [CrossRef]
11. Zaghib, K.; Charest, P.; Dontigny, M.; Guerfi, A.; Lagacé, M.; Mauger, A.; Kopec, M.; Julien, C.M. $LiFePO_4$: From molten ingot to nanoparticles with high-rate performance in Li-ion batteries. *J. Power Sources* **2010**, *195*, 8280–8288. [CrossRef]

12. Wang, Z.; Wu, F.; Su, Y.F.; Bao, L.-Y.; Chen, L.; Li, N.; Chen, S. Preparation and characterization of $x$$Li_2MnO_3$·(1–$x$) $Li[Ni_{1/3}Mn_{1/3}Co_{1/3}]O_2$ cathode materials for lithium-ion batteries. *Acta Phys. Chim. Sin.* **2012**, *28*, 823–830.
13. Hashem, A.M.; Abdel-Ghany, A.E.; El-Tawil, R.; Bhaskar, A.; Hunzinger, B.; Ehrenberg, H.; Mauger, A.; Julien, C.M. Urchin-like α-MnO_2 formed of nano-needles for high-performance lithium batteries. *Ionics* **2016**, *22*, 2263–2271. [CrossRef]
14. Feng, L.; Xuan, Z.; Zhao, H.; Bai, Y.; Guo, J.; Su, C.-W.; Chen, X. MnO_2 prepared by hydrothermal method and electrochemical performance as anode for lithium-ion battery. *Nanoscale Res. Lett.* **2014**, *9*, 290. [CrossRef] [PubMed]
15. Jarvis, K.A.; Deng, Z.; Allard, L.F.; Manthiram, A.; Ferreira, P.J. Atomic structure of a lithium-rich layered oxide material for lithium-ion batteries: Evidence of a solid solution. *Chem. Mater.* **2011**, *23*, 3614–3621. [CrossRef]
16. Zhang, X.; Mauger, A.; Lu, Q.; Groult, H.; Perrigaud, L.; Gendron, F.; Julien, C.M. Synthesis and characterization of $LiNi_{1/3}Mn_{1/3}Co_{1/3}O_2$ by wet chemical method. *Electrochim. Acta* **2010**, *55*, 6440–6449. [CrossRef]
17. Wu, H.M.; Rao, C.V.; Rambabu, B. Electrochemical performance of $LiNi_{0.5}Mn_{1.5}O_4$ prepared by improved solid state method as cathode in hybrid supercapacitor. *Mater. Chem. Phys.* **2009**, *116*, 532–535. [CrossRef]
18. Suchanek, W.L.; Riman, R.E. Hydrothermal synthesis of advanced ceramic powders. *Adv. Sci. Technol.* **2006**, *45*, 184–193. [CrossRef]
19. Cao, G.; Liu, D. Template-based synthesis of nanorod, nanowire, and nanotube arrays. *Adv. Colloid. Interface Sci.* **2008**, *136*, 45–64. [CrossRef] [PubMed]
20. Hwang, B.-J.; Hsu, K.-F.; Hu, S.-K.; Cheng, M.-Y.; Chou, T.-C.; Tsay, S.-Y.; Santhanam, R. Template-free reverse micelle process for the synthesis of a rod-like $LiFePO_4$/C composite cathode material for lithium batteries. *J. Power Sources* **2009**, *194*, 515–519. [CrossRef]
21. Kwon, S.J.; Kim, C.W.; Jeong, W.T.; Lee, K.S. Synthesis and electrochemical properties of olivine $LiFePO_4$ as a cathode material prepared by mechanical alloying. *J. Power Sources* **2004**, *137*, 93–99. [CrossRef]
22. Liao, X.Z.; Ma, Z.F.; Wang, L.; Zhang, X.-M.; Jiang, Y.; He, Y.-S. A novel synthesis route for $LiFePO_4$/C cathode materials for lithium-ion batteries. *Electrochem. Solid-State Lett.* **2004**, *7*, A522–A525. [CrossRef]
23. Franger, S.; Bourbon, C.; Le Cras, F. Optimized lithium iron phosphate for high-rate electrochemical applicatioons. *J. Electrochem. Soc.* **2004**, *151*, A1024–A1027. [CrossRef]
24. Kim, J.-K.; Choi, J.-W.; Cheruvally, G.; Kim, J.-U.; Ahn, J.-H.; Cho, G.-B.; Ahn, H.-J. A modified mechanical activation synthesis for carbon-coated $LiFePO_4$ cathode in lithium batteries. *Mater. Lett.* **2007**, *61*, 3822–3825. [CrossRef]
25. Kosova, N.V.; Devyatkina, E.T. Synthesis of nanosized materials for lithium-ion batteries by mechanical activation. Studies of their structure and properties. *Russian J. Electrochem.* **2012**, *48*, 320–329. [CrossRef]
26. Kosova, N.V.; Devyatkina, E.T. A new approach to prepare nanosized cathode materials. *ECS Trans.* **2010**, *25*, 19–25.
27. Liu, D.; Trottier, J.; Charest, P.; Fréchette, J.; Guerfi, A.; Mauger, A.; Julien, C.M.; Zaghib, K. Effect of nano $LiFePO_4$ coating on $LiMn_{1.5}Ni_{0.5}O_4$ 5 V cathode for lithium ion batteries. *J. Power Sources* **2012**, *204*, 127–132. [CrossRef]
28. Whittingham, M.S. Lithium batteries and cathode materials. *Chem. Rev.* **2004**, *104*, 4271–4301. [CrossRef] [PubMed]
29. Julien, C.; Haro-Poniatowski, E.; Camacho-Lopez, M.A.; Escobar-Alarcon, L.; Jimenez-Jarquin, J. Growth of V_2O_5 thin films by pulsed laser deposition and their applications in lithium microbatteries. *Mater. Sci. Eng. B* **1999**, *65*, 170–176. [CrossRef]
30. Bouhedja, L.; Castro-Garcia, S.; Livage, J.; Julien, C. Lithium intercalation in α'-$Na_yV_2O_5$ synthesized via the hydrothermal route. *Ionics* **1998**, *4*, 227–233. [CrossRef]
31. Tompsett, D.A.; Islam, M.S. Electrochemistry of hollandite α-MnO_2: Li-ion and Na-ion insertion and Li_2O incorporation. *Chem. Mater.* **2013**, *25*, 2515–2526. [CrossRef]
32. Hashem, A.M.; Abuzeid, H.M.; Abdel-Latif, A.M.; Abbas, H.M.; Ehrenberg, H.; Indris, S.; Mauger, A.; Groult, H.; Julien, C.M. MnO_2 nanorods prepared by redox reaction as cathodes in lithium batteries. *ECS Trans.* **2013**, *50–24*, 125–130. [CrossRef]

33. Xing, L.; Cui, C.; Ma, C.; Xue, X. Facile synthesis of α-MnO_2/graphene nanocomposites and their high performance as lithium-ion battery anode. *Mater. Lett.* **2011**, *65*, 2104–2106. [CrossRef]
34. Li, B.; Rong, G.; Xie, Y.; Huang, L.; Feng, C. Low-temperature synthesis of α-MnO_2 hollow urchins and their application in rechargeable Li^+ batteries. *Inorg. Chem.* **2006**, *45*, 6404–6410. [CrossRef] [PubMed]
35. Li, L.; Nan, C.; Lu, J.; Peng, Q.; Li, Y. α-MnO_2 nanotubes: High surface area and enhanced lithium battery properties. *Chem. Commun.* **2012**, *48*, 6945–6947. [CrossRef] [PubMed]
36. Cheng, F.Y.; Zhao, J.Z.; Song, W.; Li, C.; Ma, H.; Chen, J.; Shen, P. Facile controlled synthesis of MnO_2 nanostructures of novel shapes and their applications in batteries. *Inorg. Chem.* **2006**, *45*, 2038–2044. [CrossRef] [PubMed]
37. Kijima, N.; Takahashi, Y.; Akimoto, J.; Awaka, J. Lithium ion insertion and extraction reactions with hollandite-type manganese dioxide free from any stabilizing cations in its tunnel cavity. *J. Solid State Chem.* **2005**, *178*, 2741–2750. [CrossRef]
38. Yang, Y.; Xiao, L.; Zhao, Y.; Wang, F. Hydrothermal synthesis and electrochemical characterization of α-MnO_2 nanorods as cathode material for lithium batteries. *Int. J. Electrochem. Sci.* **2008**, *3*, 67–74.
39. Hill, L.I.; Verbaere, A.; Guyomard, D. MnO_2 (α-, β-, γ-) compounds prepared by hydrothermal-electrochemical synthesis: Characterization, morphology, and lithium insertion behavior. *J. Power Sources* **2003**, *119–121*, 226–231. [CrossRef]
40. Wang, C.; Hong, J. Ionic/electronic conducting characteristics of $LiFePO_4$ cathode materials. The determining factors for high rate performance. *Electrochem. Solid-State Lett.* **2007**, *10*, A65–A69. [CrossRef]
41. Zaghib, K.; Mauger, A.; Gendron, F.; Julien, C.M. Surface effects on the physical and electrochemical properties of thin $LiFePO_4$ particles. *Chem. Mater.* **2008**, *20*, 462–469. [CrossRef]
42. Mauger, A.; Zaghib, K.; Goulet, H.; Julien, C.M. Surface and bulk properties of $LiFePO_4$: The magnetic analysis. *ECS Trans.* **2013**, *50*, 115–123. [CrossRef]
43. Aurbach, D.; Gamolsky, K.; Markovsky, B.; Salitra, G.; Gofer, Y.; Heider, U.; Oesten, R.; Schmidt, M. The study of surface phenomena related to electrochemical lithium intercalation into Li_xMO_y host materials (M = Ni, Mn). *J. Electrochem. Soc.* **2000**, *147*, 1322–1331. [CrossRef]
44. Hashem, A.M.A.; Abdel-Ghany, A.E.; Eid, A.E.; Trottier, J.; Zaghib, K.; Mauger, A.; Julien, C.M. Study of the surface modification of $LiNi_{1/3}Co_{1/3}Mn_{1/3}O_2$ cathode material for lithium ion battery. *J. Power Sources* **2011**, *196*, 8632–8637. [CrossRef]
45. Amalraj, S.F.; Sharon, D.; Talianker, M.; Julien, C.M.; Burlaka, L.; Lavi, R.; Zhecheva, E.; Markovsky, B.; Zinigrad, E.; Kovacheva, D.; et al. Study of the nanosized Li_2MnO_3: Electrochemical behavior, structure, magnetic properties, and vibrational modes. *Electrochim. Acta* **2013**, *97*, 259–270. [CrossRef]
46. Kalyani, P.; Chitra, S.; Mohan, T.; Gopukumar, S. Lithium metal rechargeable cells using Li_2MnO_3 as the positive electrode. *J. Power Sources* **1999**, *80*, 103–106. [CrossRef]